

## Article

# Effect of TiB<sub>2</sub> Addition on the Microstructure and Mechanical Properties of Laser-Directed Energy Deposition TiAl Alloy

Yancheng Yang<sup>1</sup>, Yi Hu<sup>1,2</sup>, Hongyan Chen<sup>1,2</sup>, Yu Li<sup>1,2</sup>, Jiawei Wang<sup>1</sup>, Xu Cheng<sup>1,2</sup>, Haibo Tang<sup>1,2,\*</sup>, Xianzhe Ran<sup>1,2</sup> and Dong Liu<sup>3</sup>

<sup>1</sup> National Engineering Laboratory of Additive Manufacturing for Large Metallic Components, Beijing 100191, China; yangyancheng@buaa.edu.cn (Y.Y.); huyi@buaa.edu.cn (Y.H.); chenhongyan@buaa.edu.cn (H.C.); liyu@buaa.edu.cn (Y.L.); wangjiawei@buaa.edu.cn (J.W.); chengxu@buaa.edu.cn (X.C.); rxianzhe@buaa.edu.cn (X.R.)

<sup>2</sup> Research Institute for Frontier Science, Beihang University, Beijing 100191, China

<sup>3</sup> Beijing Yuding Additive Manufacturing Research Institute Co., Ltd., Beijing 100096, China; liudong@buaa.edu.cn

\* Correspondence: tanghb@buaa.edu.cn

**Abstract:** The microstructure characteristics of TiAl alloy prepared by laser-directed energy deposition (L-DED) are coarse columnar grains parallel to the building direction, which results in serious mechanical properties and anisotropy and limits its application. In the present study, TiB<sub>2</sub> can be used as an effective grain refiner due to the extremely high Q value (growth inhibition factor; the larger the Q value of an alloying element, the stronger its grain refinement effect.) of B. With TiB<sub>2</sub> addition, TiAl alloys prepared by laser-directed energy deposition with the microstructure of full equiaxed grains were obtained, and the grain size was significantly reduced by about 30% with 0.45 wt.% TiB<sub>2</sub>. This value has been further increased to 45% when adding 0.9 wt.% TiB<sub>2</sub>. Moreover, the  $\gamma_m$  phase was nearly eliminated and the width of ( $\alpha_2 + \gamma$ ) lamellar was significantly decreased, which has positive effects on mechanical properties. Meanwhile, TiB<sub>2</sub> precipitates uniformly distribute in the matrix, as a reinforced particle to increase the hardness and compressive strength of the alloys. The microhardness of the TiAl alloy increased with the increasing content of TiB<sub>2</sub>. The addition of TiB<sub>2</sub> improved the room and high-temperature compressive properties of TiAl alloy while slightly increasing its ductility. These findings have important guiding significance for expanding the application of TiAl alloys.

**Keywords:** TiAl alloy; laser-directed energy deposition technique; TiB<sub>2</sub> addition; microstructure; mechanical properties



**Citation:** Yang, Y.; Hu, Y.; Chen, H.; Li, Y.; Wang, J.; Cheng, X.; Tang, H.; Ran, X.; Liu, D. Effect of TiB<sub>2</sub> Addition on the Microstructure and Mechanical Properties of Laser-Directed Energy Deposition TiAl Alloy. *Metals* **2024**, *14*, 533. <https://doi.org/10.3390/met14050533>

Academic Editor: Pavel Krakhmalev

Received: 18 March 2024

Revised: 16 April 2024

Accepted: 26 April 2024

Published: 30 April 2024



**Copyright:** © 2024 by the authors. Licensee MDPI, Basel, Switzerland. This article is an open access article distributed under the terms and conditions of the Creative Commons Attribution (CC BY) license (<https://creativecommons.org/licenses/by/4.0/>).

## 1. Introduction

TiAl alloy ( $\gamma$ -TiAl-based intermetallics) is an important material with excellent specific strength, modulus, and high-temperature oxidation resistance that is used to replace nickel-based superalloy components in aero-engine to improve the thrust-to-weight ratio of aircraft [1]. The TiAl alloy is mainly composed of the  $\gamma$ -TiAl phase and the  $\alpha_2$ -Ti<sub>3</sub>Al phase. The  $\gamma$ -TiAl phase has an L1<sub>0</sub> structure, belongs to the P4/mmm space group, and has lattice constants  $a = 0.401$  nm and  $c = 0.407$  nm. The  $\alpha_2$ -Ti<sub>3</sub>Al phase has a DO<sub>19</sub> structure, belongs to the P6<sub>3</sub>/mmc space group, and has lattice constants  $a = 0.578$  nm and  $c = 0.463$  nm. Compared to the  $\gamma$ -TiAl phase, the  $\alpha_2$ -Ti<sub>3</sub>Al phase has higher high-temperature tensile strength but lower plasticity. Due to the low ductility at room temperature, traditional ingot metallurgy is used to prepare TiAl components [2]. However, the slow cooling rate during the casting process will lead to a very coarse microstructure, which seriously affects the mechanical properties of the alloy [3]. Laser-directed energy deposition (L-DED) technology combines CAD (Computer-Aided Design) data with layer-by-layer deposition materials to achieve the near-net shape of components [4]. Therefore, L-DED technology

has unique advantages in the field of forming high-performance and difficult-to-machine metals such as TiAl alloys [5].

In recent years, much progress has been made by researchers in the fabrication of TiAl alloys using additive manufacturing technology [6]. Mohamma et al. [7] found that the hardness of TiAl alloys processed by LMD (laser melting deposition) was higher than that of conventional cast parts. However, because of the high cooling rate, the microstructure of the TiAl alloy prepared by LMD has coarse epitaxial  $\beta$  columnar grains and an intragranular ( $\alpha_2 + \gamma$ ) lamellar structure, which could lead to a decrease in ductility and serious anisotropy of the mechanical properties of TiAl alloys. The TiAl alloy produced by LMD's tensile strength perpendicular to the deposition direction is much higher than that parallel to the deposition direction [8]. This feature severely limits its application. At present, heat treatment and redesign of alloy composition are general methods to modify the microstructure and improve the mechanical properties of the TiAl alloy produced by L-DED [9]. Heat treatment can adjust the lamellar structure of ( $\alpha_2 + \gamma$ ); however, it is difficult to influence the morphology of prior  $\beta$  grains, and the optimization of microstructure is limited.

Titanium diboride ( $\text{TiB}_2$ ) has a significant refinement effect on the equiaxed grain structure of the as-cast TiAl alloy, which can enhance the mechanical property of the TiAl alloy by refining its microstructure [9–11]. Based on the solidification process of  $\text{TiB}_2$  in the solid-liquid phase transition of the alloy, mechanisms of microstructure refinement of TiAl by the addition of  $\text{TiB}_2$  compounds are addressed to offer heterogeneous nucleation sites [12], hinder the growth of dendrites [13,14] and promote undercooling [15] during solidification. Moreover, when  $\text{TiB}_2$  is added to TiAl alloys, it usually exists in the form of borides, and the specific boronization species will depend on the content of the B element itself and the Al content in the TiAl alloy. When the B and Al content increases, boride transitions from  $\text{TiB}$  to  $\text{TiB}_2$ , and the addition of B elements in the alloy will also cause the  $L \rightarrow \beta + \text{TiB}_2$  eutectic reaction, which will retard the grain growth by forming the secondary  $\text{TiB}_2$ , therefore effectively enhancing the performance of the TiAl alloy [12,15], e.g., Danni Huang et al. [16] showed that the addition of a certain amount of  $\text{TiB}_2$  to the TiAl alloy, prepared by using LMD, reduced the size of  $\beta$  grains of TiAl alloys with 0.5 wt.% (17.6  $\mu\text{m}$ ) and 1.0 wt.% (1.26  $\mu\text{m}$ ) was much lower than TiAl without  $\text{TiB}_2$  addition (39.8  $\mu\text{m}$ ) and eliminated the cracking with an improved room-temperature compressive strength from 1800 MPa to above 2000 MPa. In the process of preparing  $\text{TiB}_2$ -TiAl alloys with different contents, Li Wei et al. [17] prepared TiAl alloys with 1 wt.%, 2 wt.%, and 3 wt.%  $\text{TiB}_2$  contents by using the selective laser melting (SLM) technique, and he found that the average grain size of the alloy gradually decreased from 8.53  $\mu\text{m}$  to 7.26, 6.28, and 5.39  $\mu\text{m}$ , respectively, and the nano-hardness of TiAl alloys with 1 wt.% (9.96 GPa), 2 wt.% (10.57 GPa), and 3 wt.%  $\text{TiB}_2$  (9.98 GPa) by using the SLM was higher than TiAl alloys without  $\text{TiB}_2$  addition (9.38 GPa). Publications also show that the refinement effect of the alloy manufactured by L-DED is closely dependent on the additional amount of  $\text{TiB}_2$  [18]; too low or too high concentrations of B in the TiAl alloy will not give comprehensive mechanical properties [19,20]. Studies have shown that the grain size of TiAl alloy manufactured by SLM gradually decreased with the increase of  $\text{TiB}_2$  addition, and the tensile strength and yield strength increased, but when  $\text{TiB}_2$  addition was too high, it had a negative effect on plasticity.

However, there is a lack of satisfactory work on the regulation of microstructure and improvement of mechanical anisotropy of the TiAl alloy prepared by L-DED. Hence, to further understand the influence of  $\text{TiB}_2$  addition on the microstructure and mechanical properties of TiAl alloy, in this paper, TiAl alloy, a 0.45 wt.%  $\text{TiB}_2$ -TiAl alloy, and a 0.9 wt.%  $\text{TiB}_2$ -TiAl alloy was designed and fabricated by the L-DED technique. Microstructure characteristics such as grain morphology and size, and type of precipitation are systematically studied to understand the mechanism of microstructure evolution and solid-state phase transformation. The hardness, nano-indentation, and room/high-temperature compression strength of the alloy are also studied. This research will provide technical support for the microstructure regulation-property optimization of TiAl alloys using the L-DED technique.

## 2. Materials and Methods

The raw materials for the experiment were TiAl-based alloy powder and TiB<sub>2</sub> powder. TiAl-based alloy powder was purchased from Shenyang Shijia Metallurgical Technology Co. (Shenyang, China), and its nominal composition was Ti-48Al-2Cr-2Nb (48 wt.%). The particle size of TiAl alloy powder was between 70 and 50 μm, and the particle size of TiB<sub>2</sub> powder was between 40 and 100 μm. Then, the TiB<sub>2</sub> addition TiAl alloy was prepared by the addition of 0.45 wt.% TiB<sub>2</sub> (0.45 wt.% TiB<sub>2</sub>-TiAl) and 0.9 wt.% TiB<sub>2</sub> (0.9 wt.% TiB<sub>2</sub>-TiAl) into TiAl alloy. Before the deposition experiment, powders were mechanically mixed for 4 h in the powder blender, and then they were dried in a vacuum drying oven at a temperature of 80 °C and held for 3 h.

The L-DED process was conducted at a laser additive manufacturing system equipped with a 10 kW fiber laser, a set of four-axis linkage CNC laths, an argon protective gas cavity (to ensure the oxygen content of the gas cavity is below 60 ppm during the laser deposition process), and a coaxial powder feeding device. The process parameters during the experiment were: laser power of 3 kW, spot diameter of 6 mm, and scanning speed of 1000 mm/min (under this parameter, the forming quality of the alloy is the best). The specimens were deposited on a hot isostatic pressing cast TiAl alloy substrate (thickness 10 mm); one specimen was prepared for each component, and after deposition, the specimens were heat treated in the furnace at 500 °C for 4 h to relieve the stress without changing the microstructure.

The microstructure of the alloy was examined by Digital Camera (Nikon D90), Optical Microscope (OM, Leica DM4000), and Scanning Electron Microscope (SEM, Apreo S LoVac). Metallographic specimens were prepared by standard mechanical polishing and etched by a Kroll agent. The grain sizes on metallographic drawings were counted by the truncated line method and averaged. The phase distribution and crystallographic texture were investigated via Electron Back-Scattered Diffraction (EBSD, JEOL JSM-7900F) and Transmission Electron Microscopy (TEM, JEOL JEM-2100, 200 KV). The collected data were processed using OIM 7 software (EDAX OIM Analysis 7.0) and Digital Micrograph software.

The specimen hardness was characterized using the hardness tester (Future-Tech FM-800 micro-Vickers) with a load of 500 g applied to the indenter of the hardness tester and a holding time of 15 s. A hardness indentation is made every certain distance along the deposition direction on the XOY surface during the test, totaling 9 hardness indentations. Select the average of 9 hardness values for the hardness of each specimen. The load-indentation depth curves of different phase regions of the specimen were measured using the nanoindentation tester (STEP500, 50 mN, 10 s). Three test points were made for different phases of each component. The three cylindrical specimens (Φ 3 × 4 mm) are taken from a laser-deposited TiAl block, as shown in Figure 1. The room and high-temperature compression tests were performed using an 8801 testing machine (loading rate 5 × 10<sup>-4</sup> s<sup>-1</sup>). The room temperature was compressed until the specimens broke, and the high temperature (760 °C) compression amount was 30%. After the compression was completed, the stress-strain curves were plotted according to the compression test data to determine the maximum compression strength and compression rate.

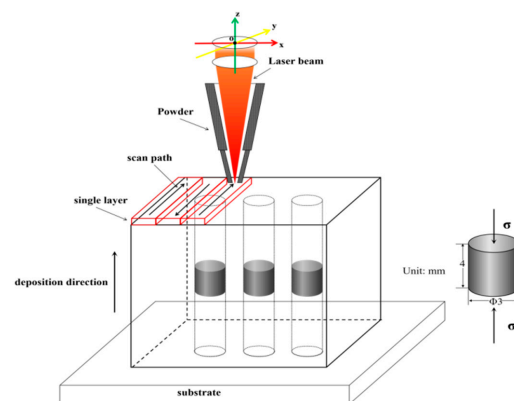


**Figure 1.** Schematic diagram of the sampling location and geometry of the compression test specimens.

### 3. Result

#### 3.1. Microstructure of Alloy with Different $TiB_2$ Addition

The microstructures of TiAl-based alloys with  $TiB_2$  additions of 0 wt.%, 0.45 wt.%, and 0.9 wt.% are shown in Figure 2. As presented in Figure 2a, the microstructure of the TiAl alloy without  $TiB_2$  addition shows a mix of columnar and equiaxed grains. As displayed in Figure 2b, with the addition of 0.45 wt.%  $TiB_2$  to the TiAl alloy, the microstructure is changed to a fully equiaxed grain structure. As shown in Figure 2c, the microstructure of 0.9 wt.%  $TiB_2$ -TiAl alloy is similar to that of 0.45 wt.%  $TiB_2$ -TiAl alloy, with a fully equiaxed grain structure but much finer grain size. The average grain size of TiAl alloy was 357  $\mu m$ ; by adding 0.45 wt.% and 0.9 wt.%  $TiB_2$  to TiAl, the grain size of the alloy decreased to about 236  $\mu m$  and 174  $\mu m$ , respectively.

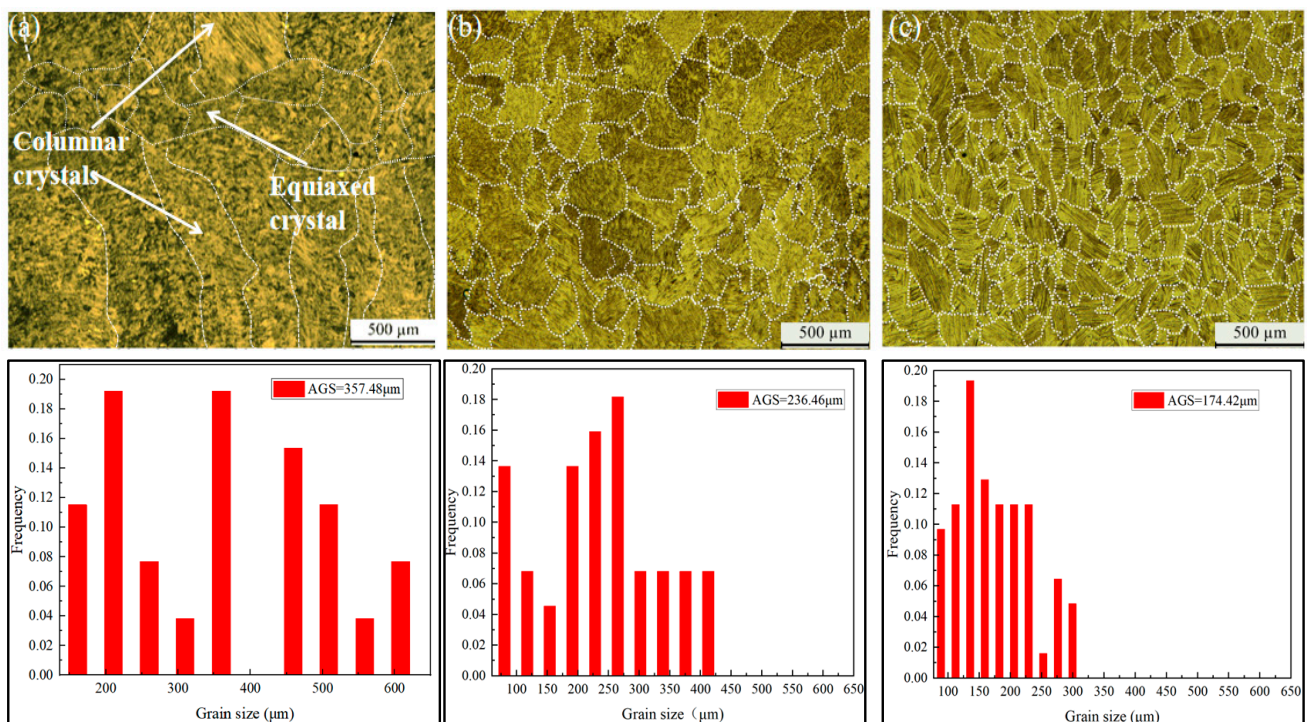


**Figure 2.** Optical images and grain size distribution diagrams of three alloys: (a) pure TiAl alloy in the deposited state; (b) 0.45 wt.%  $TiB_2$ -TiAl alloy; and (c) 0.9 wt.%  $TiB_2$ -TiAl alloy.

Figure 3 shows the BSE SEM images of specimens with different  $TiB_2$  additions. As can be seen, the TiAl alloy consists of  $(\alpha_2 + \gamma)$  lamellar and  $\gamma_m$  phases, whereas the 0.45 wt.%  $TiB_2$ -TiAl alloy and 0.9 wt.%  $TiB_2$ -TiAl alloy both have a fully  $(\alpha_2 + \gamma)$  lamellar microstructure. Meanwhile, some needle-like precipitations were also observed in specimens with  $TiB_2$  addition. Compared with the 0.45 wt.%  $TiB_2$ -TiAl alloy, the number of needle-like precipitations in the 0.9 wt.%  $TiB_2$ -TiAl alloy is larger, with a slightly longer length. EDS point scanning was performed on these needle-like precipitations and their surrounding tissues (as shown in Table 1), and the results show that the mass fraction of B element in needle-like precipitations is significantly higher than that in surrounding tissues. Further, combined with the literature [21], it can be determined that the needle-like precipitation is boride; the specific composition of these precipitated phases needs to be further examined.

EBSD analysis was performed on three alloys, as shown in Figure 4, and the results were also consistent with the SEM results. The statistical analysis of the lamellar spacing of the three compositions showed that the lamellar spacing of the TiAl alloy was 1.3  $\mu m$  on average, while for the TiAl alloy with 0.45 wt.% and 0.9 wt.%  $TiB_2$ , it was 0.9  $\mu m$  and 0.8  $\mu m$ , respectively, suggesting an obvious refinement of the  $(\alpha_2 + \gamma)$  lamellar spacing taking place.

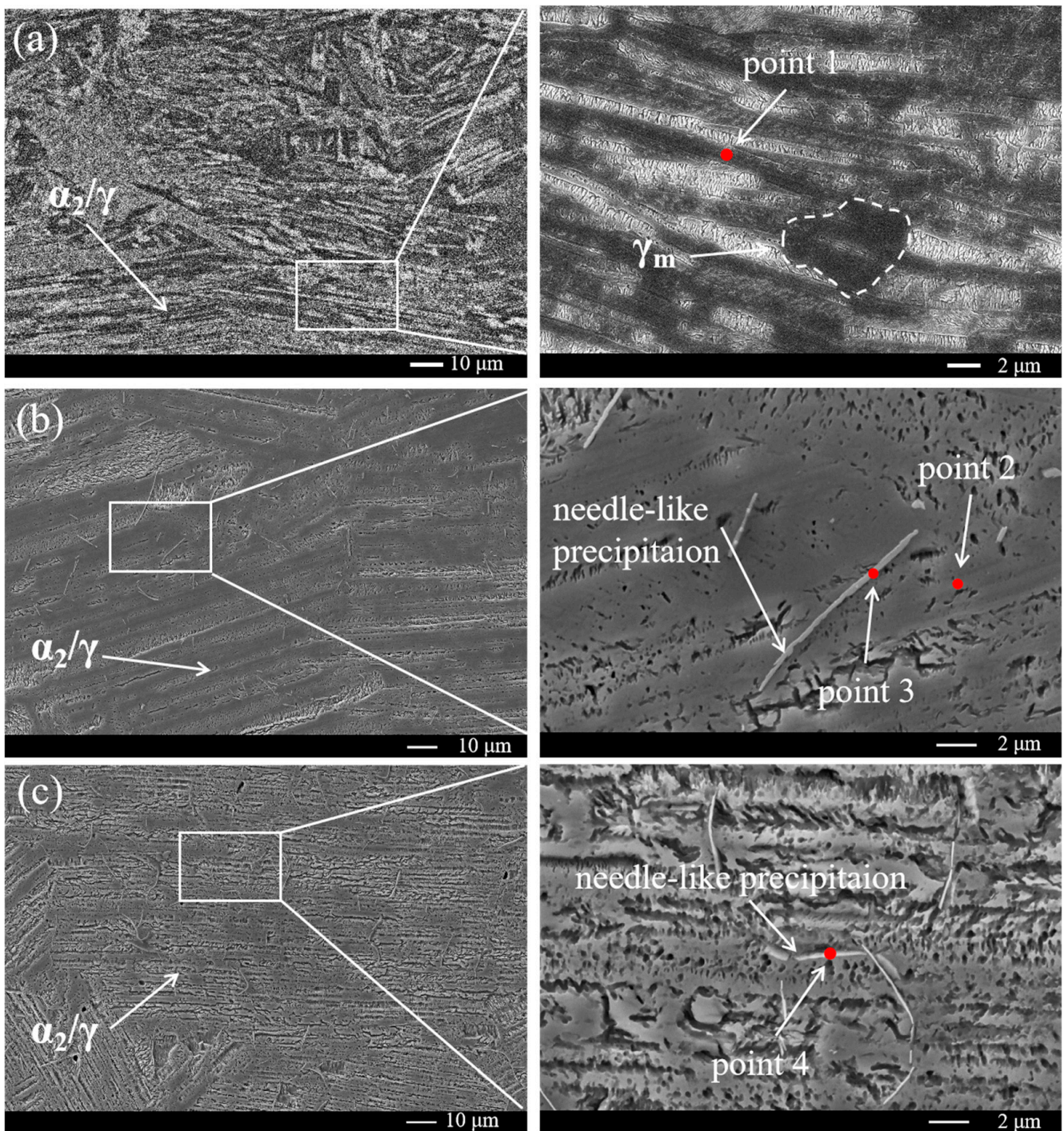


**Figure 3.** BSE SEM images of TiAl alloys with different TiB<sub>2</sub> additions: (a) pure TiAl alloy; (b) 0.45 wt.% TiB<sub>2</sub>-TiAl alloy; and (c) 0.9 wt.% TiB<sub>2</sub>-TiAl alloy.

**Table 1.** EDS results of deposited specimens with different TiB<sub>2</sub> content (wt.%).

	Ti	Al	Cr	Nb	B
1	48.9	42.7	3.5	4.9	0
2	49.8	42.3	3.4	4.5	0
3	65.4	5.6	0	0.3	28.7
4	67.4	2.1	0	0	30.5

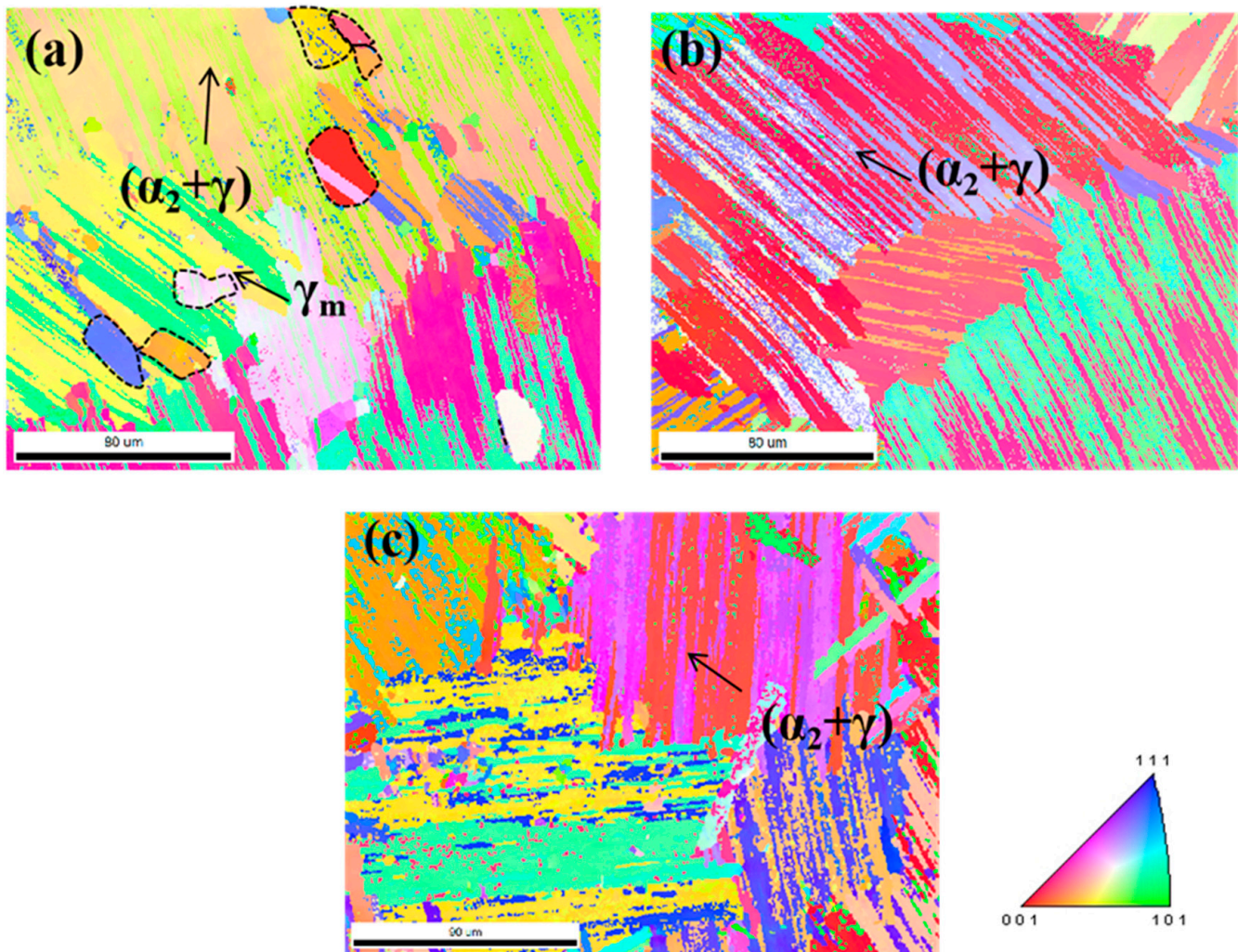


**Figure 4.** EBSD scans of TiAl alloys with different  $\text{TiB}_2$  additions: (a) pure TiAl alloy in the deposited state; (b) 0.45 wt.%  $\text{TiB}_2$ -TiAl alloy; and (c) 0.9 wt.%  $\text{TiB}_2$ -TiAl alloy.

In order to identify the type of titanium boride in this study, TEM analysis was conducted, and the results are shown in Figure 5. Figure 5a–c, respectively, correspond to the TEM bright-field images of lamellar structure, massive  $\gamma$ , and boride in the alloy. Figure 5d corresponds to the electron diffraction spots of  $\text{TiB}_2$  in the lamellae. In lamellar structure,  $\gamma$  lamellae and  $\alpha$  lamellae are alternately distributed, and the strip  $\gamma$  lamellae are between 200 and 400 nm. Figure 5c The electron diffraction pattern of the striped boride structure in the as-deposited alloy is calibrated and analyzed, and finally, it is determined that this filamentous phase is a  $\text{TiB}_2$  phase with a C32 hexagonal structure and belongs to the P6/mmm space group with lattice constants  $a = 0.303$  nm and  $c = 0.323$  nm. Primary  $\text{TiB}_2$  is usually a block structure with hexahedral characteristics [21], which can be determined as secondary  $\text{TiB}_2$  according to its strip shape. Secondary  $\text{TiB}_2$  is formed by coupling growth along a specific position of  $\beta$  phase in the eutectic reaction of  $L \rightarrow \beta + \text{TiB}_2$ , so there will be a specific orientation relationship between  $\text{TiB}_2$  and  $\beta$  phase:  $B = [1-21-3]\text{TiB}_2 // [011]\text{B}_2$ . However, no electron diffraction spots conforming to this relationship are found in the thin-plate samples, and it is speculated that the thermal conditions of rapid solidification in additive manufacturing make TiAl alloy contain a very small amount.

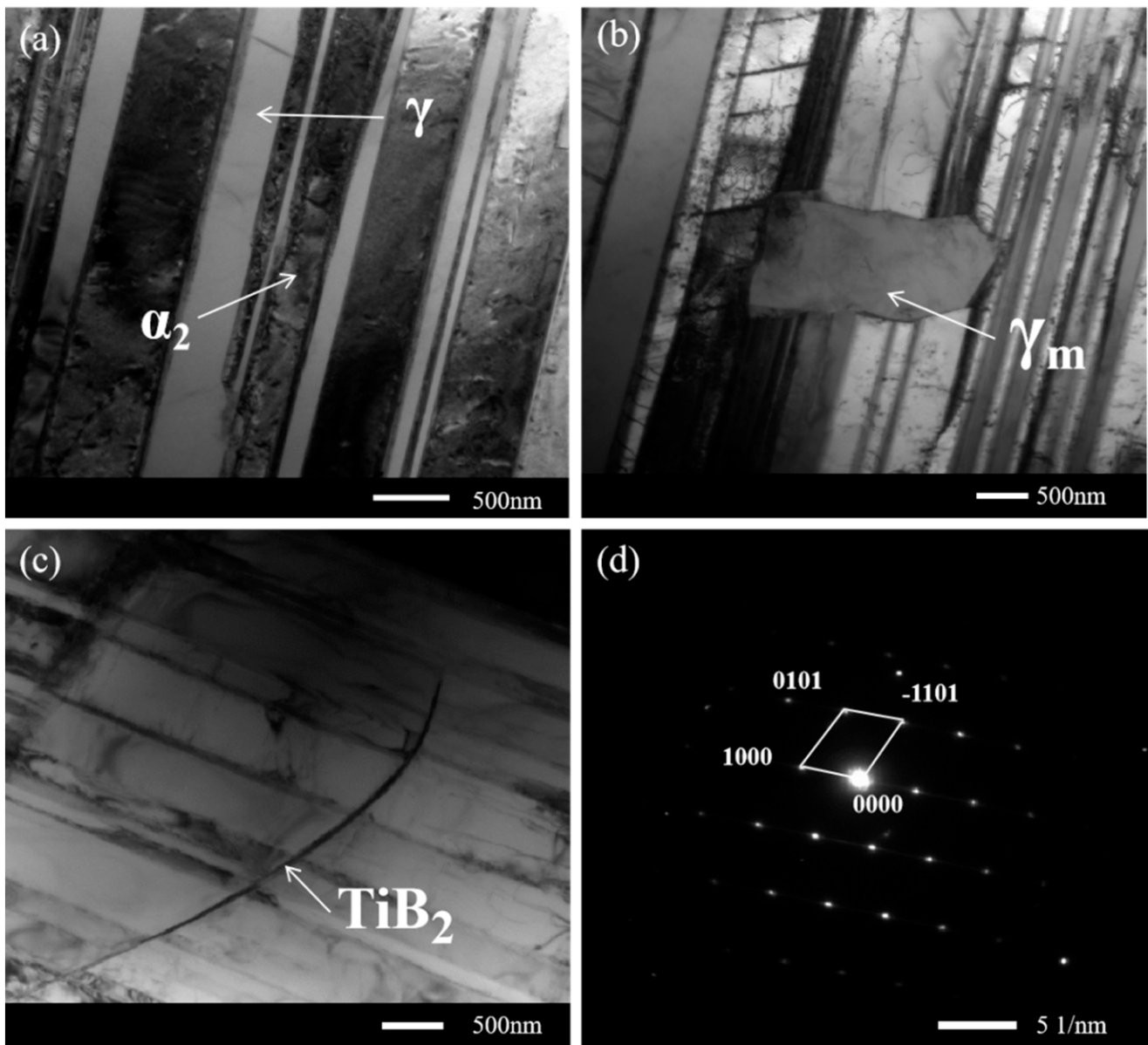


**Figure 5.** TEM images of 0.45 wt.%  $\text{TiB}_2$ -TiAl partial area: (a) lamellar structure corresponding to TEM bright field images; (b)  $\gamma_m$  structure corresponding to TEM bright field images; (c)  $\text{TiB}_2$  structure corresponding to TEM bright field images (d)  $\text{TiB}_2$  structure corresponding to electron diffraction pattern.

### 3.2. Mechanical Property

#### 3.2.1. Micro-Hardness and Nanoindentation

The hardness of TiAl alloys with  $\text{TiB}_2$  additions of 0 wt.%, 0.45 wt.%, and 0.9 wt.% is shown in Table 2. The results show that the hardness of the alloy gradually increases with the increase of  $\text{TiB}_2$  addition.

**Table 2.** Average hardness of the three alloys.

Specimen	Average Microhardness (HV)
Pure TiAl	286.0
0.45 wt.% $\text{TiB}_2$ -TiAl	303.2
0.9 wt.% $\text{TiB}_2$ -TiAl	309.2

Nanoindentation test results of  $(\alpha_2 + \gamma)$  lamellar and  $\gamma_m$  phases of the three alloys are characterized in Figure 6, and the results of indentation depth, nano-hardness (H), and elastic modulus (E) are shown in Table 3. With the increase in  $\text{TiB}_2$  addition, the  $(\alpha_2 + \gamma)$  lamellar of the alloy is refined, and the nano-hardness and elastic modulus are both increased. The H values and E values of the  $\gamma_m$  phase in pure TiAl alloy are lower than those in the  $(\alpha_2 + \gamma)$  lamellar of pure TiAl alloy. Hence, the specimens with a fully lamellar structure should have a higher hardness than the specimens with a  $(\alpha_2 + \gamma) + \gamma_m$  microstructure.

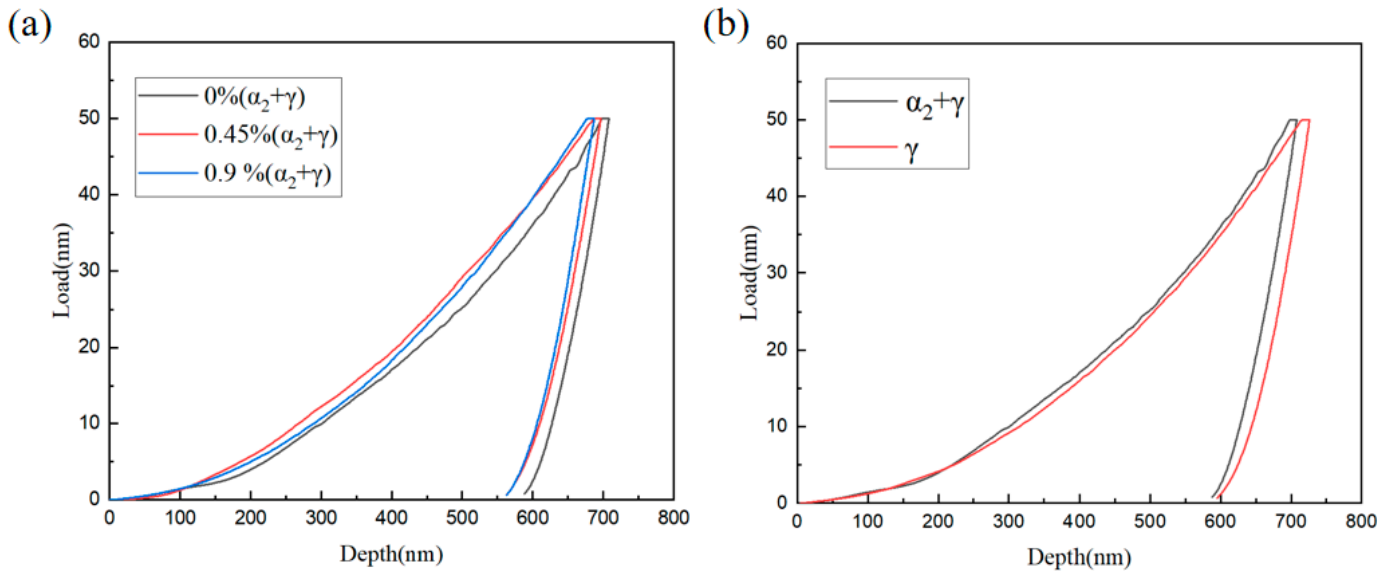


**Figure 6.** (a) Load-indentation depth curves of  $(\alpha_2 + \gamma)$  lamellar of the three alloys; (b) Load-indentation depth curves of  $(\alpha_2 + \gamma)$  lamellar and  $\gamma_m$  phases of pure TiAl alloy.

**Table 3.** Average hardness of the three composition alloys.

Affiliated Alloys	Measurement Phase	Indentation Depth ( $\mu\text{m}$ )	H (GPa)	E (GPa)
Pure TiAl	$\alpha_2 + \gamma$ lamellar	0.708	4.98	134.31
0.45 wt.% $\text{TiB}_2$ -TiAl	$\alpha_2 + \gamma$ lamellar	0.697	5.06	136.5
0.9 wt.% $\text{TiB}_2$ -TiAl	$\alpha_2 + \gamma$ lamellar	0.687	5.14	138.45
Pure TiAl	$\gamma_m$	0.726	4.69	129.0

### 3.2.2. Compression Test

The room-temperature and high-temperature compression curves of the three alloys are shown in Figure 7. As presented in Figure 7a, the compressive strength of the pure TiAl alloy is the lowest, which is 1596 MPa. However, the yield strength is the highest, at 773 MPa. Additionally, the engineering strain of the specimen is about 28% when it reaches its maximum compressive strength. The compressive strength of 0.45 wt.%  $\text{TiB}_2$ -TiAl alloy was significantly higher than that of pure TiAl alloy, which is about 1771 MPa. However, the yield strength is the highest, at 773 MPa. Additionally, the engineering strain of the specimen when it reached its maximum compressive strength was nearly 32%. The specimen of 0.9 wt.%  $\text{TiB}_2$ -TiAl alloy had the highest compressive strength, which is about 1970 MPa with an engineering strain of 33%, and the yield strength has been improved compared to 0.45 wt.%  $\text{TiB}_2$ -TiAl alloy, which is 698 MPa. The increase in strength and plasticity may be due to grain refinement induced by  $\text{TiB}_2$  addition. There is no sudden breakage of the specimen observed in alloys at the test temperature of 760 °C with the set engineering strain of 30%. The high-temperature compression curves of the specimens are shown in Figure 7b. The yield strengths of the alloy with 0 wt.%, 0.45 wt.%, and 0.9 wt.%  $\text{TiB}_2$  additions are

395 MPa, 463 MPa, and 513 MPa, respectively. It was obvious to find that the high-temperature yield strengths of the alloys increased with the increase in TiB<sub>2</sub> addition.

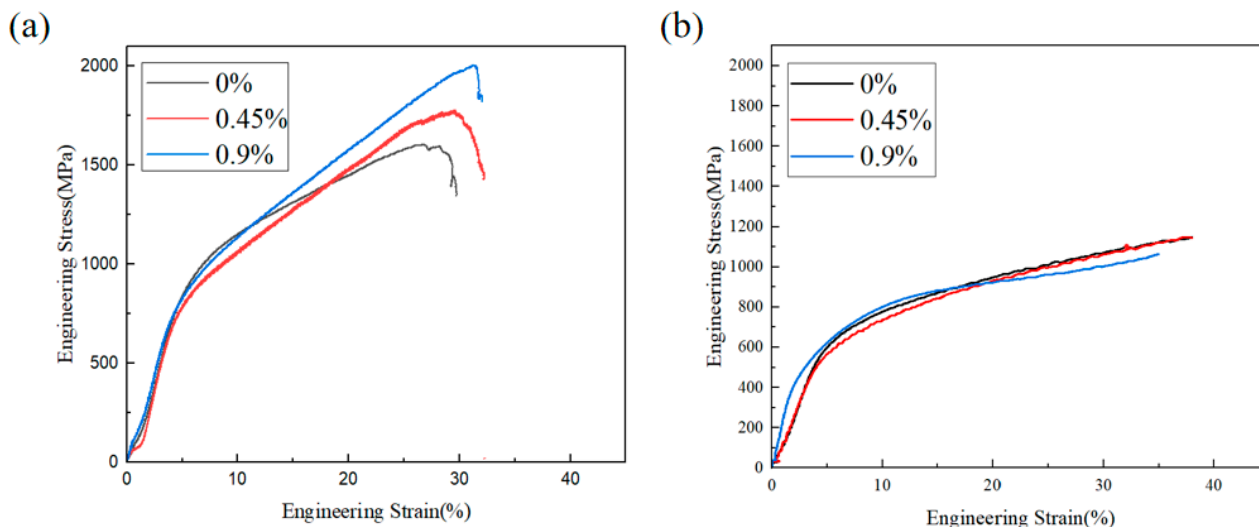


**Figure 7.** (a) Room temperature compression curves of the three alloys; (b) High-temperature compression curves of the three alloys.

## 4. Discussion

### 4.1. Microstructure Evolution

#### 4.1.1. The Equivalation and Refinement Mechanism of Grain

After the addition of TiB<sub>2</sub>, the microstructure of the TiAl alloy changed from a mixture of columnar and equiaxed grains to fully equiaxed grains, and the equiaxed grains can be further refined with the increase in TiB<sub>2</sub> addition, as shown in Figure 2. Because the processing parameters of the three types of specimens during L-DED are the same, the grain refinement of the alloy could be attributed to the TiB<sub>2</sub> addition, which effectively influences the solidification behavior of the TiAl alloy. As it was known, the solidification of the alloy is closely related to the temperature gradient and solidification rate, and the solidification structure of the alloy can be predicted based on the following Equation (1) [22].

$$\begin{aligned} \frac{G^n}{V} &= a \cdot \left[ \sqrt[3]{\frac{-4\pi N_0}{3 \ln(1-\phi)} \cdot \frac{1}{n+1}} \right]^n = K_C, \phi = 0.0066 \\ \frac{G^n}{V} &= a \cdot \left[ \sqrt[3]{\frac{-4\pi N_0}{3 \ln(1-\phi)} \cdot \frac{1}{n+1}} \right]^n = K_E, \phi = 0.49 \end{aligned} \quad (1)$$

where  $G$  is the temperature gradient,  $V$  is the solidification rate,  $N_0$  is the number of non-uniformly shaped nucleation sites available per unit volume,  $\phi$  is the volume fraction of newly formed nuclei in the undercooling zone at the front of the solid-liquid interface, and  $a$  and  $n$  are material-dependent constants. When  $\phi$  is less than 0.0066, the growth of equiaxed grains at the solid-liquid interface front is completely suppressed, and the formation of columnar grains is enhanced. When  $\phi$  is greater than 0.49, the growth is completely in the form of equiaxed grains. The effect of adding TiB<sub>2</sub> on the ratio of temperature gradient and growth rate is mainly manifested in two aspects: firstly, it affects the volume fraction  $\phi$  of newly formed nuclei in the undercooling zone at the front of the solid-liquid interface; secondly, it affects the number of nuclei sites  $N_0$  per unit volume. When the content of B in the liquid phase reaches its solubility, a boron-rich layer is formed in the liquid beside the solidification fronts. Such a rich boron layer forms a constitutional undercooling area, which could prevent solid-phase fluid growth, leading to an increase in the volume fraction of newly formed nuclei  $\phi$  [23]. As the content of TiB<sub>2</sub> increases, the structural undercooling reaches a higher level due to the transition of boron from the solid phase to the liquid phase on the solidification front. In the solid phase, homogeneous nucleation occurs, which increases the nucleation density, causing grain refinement. Moreover, there are excellent

lattice mismatches between the reinforcing  $\text{TiB}_2$  phase and the  $\gamma$ -TiAl and  $\alpha_2$  phases in the alloy, so  $\text{TiB}_2$  can be used as a heterogeneous nucleation site in the liquid phase during the solidification process of the material, which promotes heterogeneous nucleation and increases the number of nucleation sites  $N_0$ . The increase in nucleation volume fraction  $\phi$  and heterogeneous nucleation sites  $N_0$  promotes equiaxed grain formation [22].

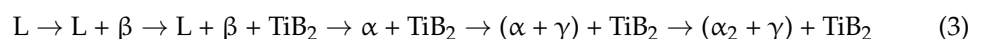
Because the grain structure of both 0.45 wt.%  $\text{TiB}_2$ -TiAl and 0.9 wt.%  $\text{TiB}_2$ -TiAl alloys are both equiaxed, based on Equation (1), their  $\phi$  value is 0.49. The specimen of 0.9 wt.%  $\text{TiB}_2$ -TiAl alloy has a finer grain size than that of 0.45 wt.%  $\text{TiB}_2$ -TiAl alloy, which suggests that the addition of  $\text{TiB}_2$  can further inhibit grain growth. As it was known, the growth inhibition factor  $Q$  [23] can be calculated in Equation (2).

$$Q = \sum m_1 C_0 (k - 1) \quad (2)$$

where  $m_1$  is the liquid phase line gradient,  $C_0$  is the alloy composition, and  $k$  is the partition coefficient. Combined with the Ti-Al, Ti-Cr, Ti-Nb, and Ti-B binary phase diagrams [24,25], a  $Q$  value of 1.07245 can be calculated for the specimen 0.45 wt.%  $\text{TiB}_2$ -TiAl alloy and 1.3987 for the 0.9 wt.%  $\text{TiB}_2$ -TiAl alloy. The grain growth inhibition factor value  $Q$  increases with the rise of B contents with finer grain size.

#### 4.1.2. The Transition Mechanism of Phase

As shown in Figure 3, with the increase in  $\text{TiB}_2$  addition, the volume fraction of the  $\gamma_m$  phase gradually decreased. The formation of  $(\alpha_2 + \gamma)$  lamellar is controlled by the diffusion of atoms [26], while  $\gamma_m$  is formed by massive transformation [27]. For the TiAl alloy, the solidification path of the TiAl alloy with  $\text{TiB}_2$  is [28] as follows:



The addition of  $\text{TiB}_2$  will restrain the epitaxial growth of columnar grain in the alloy, promoting the formation of fine  $\beta$ -dendrites, increasing the area of diffusion, and reducing the distance of diffusion [29]. During solid-phase transformation,  $\text{TiB}_2$  can act as the heterogeneous nucleation site for the  $\alpha$  phase, which refines the microstructure of the alloy. From Figure 4, it can be seen that the  $\text{TiB}_2$  in the TiAl alloy is needle-like, which is mostly distributed between different  $(\alpha_2 + \gamma)$  lamellar and within the lamellar. The distribution at the lamellar junction may be due to the addition of  $\text{TiB}_2$ , which causes the liquid-solid interface front to be undercooled, and the  $\text{TiB}_2$  precipitates along the grain boundary during the solidification of the alloy [24]. The distribution inside the lamellar may be due to the precipitation of  $\text{TiB}_2$  during solidification after it reaches solubility. Hence, the primary  $\text{TiB}_2$  usually has a blocky structure with hexahedral characteristics, and the secondary  $\text{TiB}_2$  always has a needle-like morphology [30].

#### 4.2. Effect of $\text{TiB}_2$ on Mechanical Properties of Alloy

Adding  $\text{TiB}_2$  can effectively refine the microstructure of the TiAl alloy with enhanced hardness. Research indicate that the spacing of  $(\alpha_2 + \gamma)$  lamellar directly affects the hardness of TiAl alloy, and the smaller the  $(\alpha_2 + \gamma)$  lamellar spacing, the larger the areas of interfaces with a stronger hindering effect for dislocation movement, resulting in higher hardness. The corresponding relationship between lamellar spacing and microhardness in TiAl alloy is shown as follows [31]:

$$H = H_{v0} + k\lambda^{-0.5} \quad (4)$$

where  $H_{v0}$  is the stress required for dislocation motion through the crystal (MPa),  $k$  is the Hall-Petch coefficient ( $\text{MPa} \times \mu\text{m}^{1/2}$ ), and  $\lambda$  is the lamellar spacing ( $\mu\text{m}$ ). The relationship between microhardness and  $(\alpha_2 + \gamma)$  lamellar spacing can be obtained by measuring the lamellar spacing at the indentation location:

$$H = 204.68 + 93.52\lambda^{-0.5}, r^2 = 0.991 \quad (5)$$

As shown in Figure 7, the TiAl alloy with 0.45 and 0.9 wt.% TiB<sub>2</sub> showed higher compressive strength and strain than the pure TiAl alloy, which indicates that the addition of TiB<sub>2</sub> could improve the compressive strength and ductility of the material. There are two reasons for this: firstly, the addition of TiB<sub>2</sub> refines the grains, reduces the lamellar spacing, and increases the volume fraction of ( $\alpha_2 + \gamma$ ) lamellar with enhanced compressive strength; secondly, the needle-like TiB<sub>2</sub> precipitates in the alloy can play a role in second-phase strengthening.

As it was known, work hardening can reflect the ability of the material to resist further deformation in uniform plastic deformation, and the work hardening capacity (Hc) of the material is characterized as [32]:

$$Hc = (\delta_{ucs} - \delta_y) / \delta_y \quad (6)$$

where  $\delta_y$  is the yield strength and  $\delta_{ucs}$  is the compressive strength. The work-hardening abilities of the three alloys can be calculated, which were 1.06, 1.81, and 1.82 for pure TiAl, 0.45 wt.% TiB<sub>2</sub>-TiAl, and 0.9 wt.% TiB<sub>2</sub>-TiAl. This result indicated that the work-hardening ability of the alloys gradually increased with the increase in TiB<sub>2</sub> addition.

## 5. Conclusions

In this paper, TiAl alloy specimens with different TiB<sub>2</sub> additions were prepared by the L-DED technique. The influence of TiB<sub>2</sub> addition on the grain morphology, phase component, microhardness, nanoindentation, and room- and high-temperature compressive properties of the alloy was discussed, and the main conclusions are as follows:

- (1) The addition of TiB<sub>2</sub> can promote equivalence and grain refinement in the TiAl alloy prepared by L-DED. The grain morphology of the Ti-Al alloy without TiB<sub>2</sub> had alternating columnar and equiaxed grains, and the transverse size of columnar grains was 245  $\mu\text{m}$ . However, the grain morphology of 0.45 wt.% TiB<sub>2</sub>-TiAl and 0.9 wt.% TiB<sub>2</sub>-TiAl alloys was nearly fully equiaxed, with an average grain size of 168  $\mu\text{m}$  and 133  $\mu\text{m}$ , respectively. Compared to no TiB<sub>2</sub> addition, it has decreased by 30% and 45%.
- (2) The addition of TiB<sub>2</sub> promoted the transformation of the alloy structure from a structure consisting of ( $\alpha_2 + \gamma$ ) lamellar and  $\gamma_m$  to a full ( $\alpha_2 + \gamma$ ) lamellar structure with refined lamellar spacing. The lamellar spacing was 1.3  $\mu\text{m}$  for TiAl, 0.9  $\mu\text{m}$  for 0.45 wt.% TiB<sub>2</sub>-TiAl, and 0.8  $\mu\text{m}$  for 0.9 wt.% TiB<sub>2</sub>-TiAl.
- (3) With the increase in TiB<sub>2</sub> content, the grains were refined, the volume fraction of ( $\alpha_2 + \gamma$ ) lamellar increased, and the lamellar spacing was decreased, which made the hardness, room temperature, and high-temperature compressive strength and ductility of the alloy gradually increase.

The introduction of TiB<sub>2</sub> as a grain refiner has exerted a profound influence on the microstructure and properties of TiAl alloys fabricated via laser-directed energy deposition (L-DED) technology. This study has uncovered the pivotal role of TiB<sub>2</sub> in optimizing the microstructure and enhancing the performance of TiAl alloys. These findings not only deepen our understanding of the mechanistic role of TiB<sub>2</sub> in TiAl alloys but also offer invaluable insights and guidance for the design and development of high-performance TiAl alloys with improved characteristics. Consequently, this research holds promise for facilitating the broader application of TiAl alloys in critical sectors such as aerospace, energy, and automotive manufacturing.

**Author Contributions:** Conceptualization, Y.Y.; Methodology, Y.Y., X.C. and X.R.; Investigation, Y.Y., Y.H., H.C. and Y.L.; Data curation, Y.Y., J.W., X.R. and D.L.; Visualization, Y.Y.; Formal analysis, Y.Y. and J.W.; Writing-original draft, Y.Y.; Writing-review and editing, Y.Y., H.C., Y.L. and X.C.; Resources, X.C.; Project administration, X.C. and H.T.; Supervision, X.C. and H.T.; Funding acquisition, H.T.; Project administration, H.T.; Experimental guidance, X.R. and D.L. All authors have read and agreed to the published version of the manuscript.

**Funding:** This study is supported by the National Science and Technology Major Project of China (No. 2019-VII-0003-0143), Basic and Applied Basic Research Foundation of Guangdong Province of China (No. 2020B0301030001).

**Data Availability Statement:** The original contributions presented in the study are included in the article, further inquiries can be directed to the corresponding author.

**Conflicts of Interest:** Author Dong Liu is employed by the company Beijing Yuding Additive Manufacturing Research Institute Co., Ltd. The remaining authors declare that the research was conducted in the absence of any commercial or financial relationships that could be construed as a potential conflict of interest.

## References

1. Li, J.; Chen, C.; Squartini, T.; He, Q. A study on wear resistance and microcrack of the Ti<sub>3</sub>Al/TiAl+ TiC ceramic layer deposited by laser cladding on Ti-6Al-4V alloy. *Appl. Surf. Sci.* **2010**, *257*, 1550–1555. [CrossRef]
2. Wang, H.; Xie, G.; Jia, Y.; Yao, H.; Xiao, S.; Chen, Y.; Han, J.; Wang, T. Solidification Microstructure Evolution and Mechanical Properties of Casting Ti-48Al-2Cr-2Nb-(Ni, TiB<sub>2</sub>) Alloy. *Rare Met. Mater. Eng.* **2022**, *51*, 2316–2322.
3. Chen, Y.; Kong, F.; Tian, J.; Chen, Z.; Xiao, S. Recent developments in engineering gamma-TiAl intermetallics. *Trans. Nonferrous Met. Soc. China* **2002**, *12*, 605–609.
4. DebRoy, T.; Wei, H.L.; Zuback, J.S.; Mukherjee, T.; Elmer, J.W.; Milewski, J.O.; Beese, A.M.; Wilson-Heid, A.D.; De, A.; Zhang, W. Additive manufacturing of metallic components—Process, structure and properties. *Prog. Mater. Sci.* **2018**, *92*, 112–224. [CrossRef]
5. Gu, D.D.; Meiners, W.; Wissenbach, K.; Poprawe, R. Laser additive manufacturing of metallic components: Materials, processes and mechanisms. *Int. Mater. Rev.* **2012**, *57*, 133–164. [CrossRef]
6. Soliman, H.A.; Elbestawi, M. Titanium aluminides processing by additive manufacturing—A review. *Int. J. Adv. Manuf. Technol.* **2022**, *119*, 5583–5614. [CrossRef]
7. Mohammad, A.; Al-Ahmari, A.M.; AlFaify, A.; Mohammed, M.K. Effect of melt parameters on density and surface roughness in electron beam melting of gamma titanium aluminide alloy. *Rapid Prototyp. J.* **2017**, *23*, 474–485. [CrossRef]
8. Zhang, X.; Li, C.; Zheng, M.; Ye, Z.; Yang, X.; Gu, J. Anisotropic tensile behavior of Ti-47Al-2Cr-2Nb alloy fabricated by direct laser deposition. *Addit. Manuf.* **2020**, *32*, 101087. [CrossRef]
9. Chen, Y.; Chen, Y.; Tian, J.; Kong, F.; Xiao, S.; Xu, L. Development and research status of investment casting TiAl-based alloys. *Rare Met. Mater. Eng.* **2009**, *38*, 554–558.
10. Dong, L.; Cui, Y.; Yang, R. Effects of B or C on the macro-and micro-structures of cast near gamma TiAl alloys. *Acta Metall.* **2002**, *38*, 643–646.
11. Ouadah, O.; Merad, G.; Abdelkader, H.S. Energetic segregation of B, C, N, O at the  $\gamma$ -TiAl/ $\alpha$ -Ti<sub>3</sub>Al interface via DFT approach. *Vacuum* **2021**, *186*, 110045. [CrossRef]
12. Han, J.; Xiao, S.; Tian, J.; Chen, Y.; Xu, L.; Wang, X.; Jia, Y.; Du, Z.; Cao, S. Grain refinement by trace TiB<sub>2</sub> addition in conventional cast TiAl-based alloy. *Mater. Charact.* **2015**, *106*, 112–122. [CrossRef]
13. Kim, M.; Oh, M.; Lee, J.; Inui, H.; Yamaguchi, M.; Wee, D. Composition and growth rate effects in directionally solidified TiAl alloys. *Mater. Sci. Eng. A* **1997**, *239*, 570–576. [CrossRef]
14. Fan, L.; Kou, H.; Zhong, H.; Zhang, T.; Li, J. Effects of Boron Addition on Phase Transformation of Ti47Al Alloy. *Rare Met. Mater. Eng.* **2014**, *43*, 115–119.
15. Sarma, B.; Chandran, K.R. Accelerated kinetics of surface hardening by diffusion near phase transition temperature: Mechanism of growth of boride layers on titanium. *Acta Mater.* **2011**, *59*, 4216–4228. [CrossRef]
16. Huang, D.; Zhou, Y.; Yao, X.; Tan, Q.; Chang, H.; Wang, D.; Lu, S.; Liu, S.; Xu, J.; Jin, S.; et al. From crack-prone to crack-free: Unravelling the roles of LaB<sub>6</sub> in a  $\beta$ -solidifying TiAl alloy fabricated with laser additive manufacturing. *Mater. Sci. Eng. A* **2022**, *861*, 144358. [CrossRef]
17. Li, W.; Yang, Y.; Liu, J.; Zhou, Y.; Li, M.; Wen, S.; Wei, Q.; Yan, C.; Shi, Y. Enhanced nanohardness and new insights into texture evolution and phase transformation of TiAl/TiB<sub>2</sub> in-situ metal matrix composites prepared via selective laser melting. *Acta Mater.* **2017**, *136*, 90–104. [CrossRef]
18. Yang, S.; Cui, C.; Cui, S.; Liu, S.; Liang, Y. Microstructure and mechanical properties of in-situ dual morphology Ti<sub>8</sub>C<sub>5</sub>/TiB<sub>2</sub> reinforced TiAl composite. *Mater. Sci. Eng. A* **2022**, *840*, 142918. [CrossRef]
19. Zhang, H.; Gao, W.; Zhang, E.; Zeng, S. Morphology Evolution and Growth Mechanism of TiB<sub>2</sub> in Ti-54Al-xB Alloys. *Acta Metall. Sin.-Chin. Ed.* **2002**, *38*, 699–702.
20. Cheng, T. The mechanism of grain refinement in TiAl alloys by boron addition—An alternative hypothesis. *Intermetallics* **2000**, *8*, 29–37. [CrossRef]
21. Hyman, M.E.; McCullough, C.; Valencia, J.J.; Levi, C.G.; Mehrabian, R. Microstructure evolution in TiAl alloys with B additions: Conventional solidification. *Metall. Trans. A* **1989**, *20*, 1847–1859. [CrossRef]
22. Zhu, Y.-Y.; Tang, H.-B.; Li, Z.; Xu, C.; He, B. Solidification behavior and grain morphology of laser additive manufacturing titanium alloys. *J. Alloys Compd.* **2019**, *777*, 712–716. [CrossRef]

23. Genc, O.; Unal, R. Development of gamma titanium aluminide ( $\gamma$ -TiAl) alloys: A review. *J. Alloys Compd.* **2022**, *929*, 167262. [[CrossRef](#)]
24. Hyman, M.E.; McCullough, C.; Levi, C.G.; Mehrabian, R. Evolution of boride morphologies in TiAl-B alloys. *Metall. Trans. A* **1991**, *22*, 1647–1662. [[CrossRef](#)]
25. Hu, B.; Jiang, Y.; Wang, J.; Yao, B.; Min, F.; Du, Y. Thermodynamic calculation of the T0 curve and metastable phase diagrams of the Ti–M (M = Mo, V, Nb, Cr, Al) binary systems. *Calphad* **2018**, *62*, 75–82. [[CrossRef](#)]
26. Hu, D.; Huang, A.; Loretto, M.H.; Wu, X. Designing TiAl alloys to transform massively during slow cooling. In Proceedings of the 11th World Conference on Titanium, Kyoto, Japan, 3–7 June 2007.
27. Clemens, H.; Mayer, S. Design, processing, microstructure, properties, and applications of advanced intermetallic TiAl alloys. *Adv. Eng. Mater.* **2013**, *15*, 191–215. [[CrossRef](#)]
28. Han, J.; Xiao, S.; Tian, J.; Chen, Y.; Xu, L.; Wang, X.; Cao, S. Microstructure characterization, mechanical properties and toughening mechanism of TiB<sub>2</sub>-containing conventional cast TiAl-based alloy. *Mater. Sci. Eng. A* **2015**, *645*, 8–19. [[CrossRef](#)]
29. Worth, B.D.; Jones, J.W.; Allison, J.E. Creep deformation in near- $\gamma$  TiAl: II. influence of carbon on creep deformation in Ti-48Al-1V-0.3C. *Metall. Mater. Trans. A* **1995**, *26*, 2961–2972. [[CrossRef](#)]
30. Abdel-Hamid, A.; Hamar-Thibault, S.; Hamar, R. Crystal morphology of the compound TiB<sub>2</sub>. *Journal of crystal growth* **1985**, *71*, 744–750. [[CrossRef](#)]
31. Panov, D.O.; Sokolovsky, V.S.; Stepanov, N.D.; Zhrebtsov, S.V.; Panin, P.V.; Volokitina, E.I.; Nochovnaya, N.A.; Salishchev, G.A. Effect of interlamellar spacing on strength-ductility combination of  $\beta$ -solidified  $\gamma$ -TiAl based alloy with fully lamellar structure. *Mater. Sci. Eng. A* **2023**, *862*, 144458. [[CrossRef](#)]
32. Hirose, A.; Hasegawa, M.; Kobayashi, K.F. Microstructures and mechanical properties of TiB<sub>2</sub> particle reinforced TiAl composites by plasma arc melting process. *Mater. Sci. Eng. A* **1997**, *239*, 46–54. [[CrossRef](#)]

**Disclaimer/Publisher’s Note:** The statements, opinions and data contained in all publications are solely those of the individual author(s) and contributor(s) and not of MDPI and/or the editor(s). MDPI and/or the editor(s) disclaim responsibility for any injury to people or property resulting from any ideas, methods, instructions or products referred to in the content.